Nanoscale Phase Separation in Fe_3O_4(111) Films on Sapphire(0001) and Phase Stability of Fe_3O_4(001) Films on MgO(001) Grown by Oxygen-Plasma-Assisted Molecular Beam Expitaxy

R. F. C. Farrow *et al.*

Nanoscale phase separation in Fe_3O_4(111) films on sapphire(0001) and phase stability of Fe_3O_4(001) films on MgO(001) grown by oxygen-plasma-assisted molecular beam epitaxy

R.F.C. Farrow, P.M. Rice, M.F. Toney, R.F. Marks, J. Hedstrom, R. Stephenson, M.J. Carey, A.J. Kellock, IBM Research Division, Almaden Research Center, 650 Harry Road, San Jose, CA 95120-6099

We report a phase instability in oxygen-plasma-assisted molecular beam epitaxy of Fe_3O_4 films on sapphire (0001) substrates. Under a wide range of growth conditions, Fe_3O_4 (111) films phase separate, on a nanometer length scale, into Fe_3O_4, FeO and metallic Fe, which is attributed to formation of the thermodynamically unstable phase FeO in the initial stages of (111) growth. In contrast, Fe_3O_4 (001) films, grown simultaneously on MgO(001) substrates, do not exhibit this phase instability. We specify growth conditions for which single-phase, epitaxial Fe_3O_4 (111) films can be grown by plasma-assisted molecular beam epitaxy or by reactive evaporation of Fe in molecular oxygen. Film orientation and phase separation strongly influence magnetic properties. Single-phase Fe_3O_4 (111) films are much more difficult to magnetize than Fe_3O_4 (001) films and phase separation makes the films even more difficult to magnetize.

PACS subject areas: 81.15H, 75.70, 81.07

Introduction

Fe_3O_4 (magnetite) has a predicted [1,2] half-metallic band structure in which only minority spin carriers occupy states at the Fermi level. This property makes Fe_3O_4 attractive as a source of fully polarized spins in magnetic tunnel junctions. Recently, Panchula et al[3] and Parkin et al[4] et al have reported that insertion of a layer of Fe_3O_4, between a normal ferromagnetic metal electrode and the tunnel barrier, in a sputtered magnetic tunnel junction, resulted in a large (>20%) magnetoresistance of opposite sign to that observed without Fe_3O_4. With Fe_3O_4, the low resistance state occurred when the magnetizations of the electrodes on each side of the barrier were *antiparallel*. This demonstrates that Fe_3O_4 acts as a spin filter, providing a source of mainly minority spin-polarized electrons. This behavior, however, was found to be sensitive to the crystallographic texture of the Fe_3O_4 film. While a highly oriented (001) texture of Fe_3O_4 led to this sign change of magnetoresistance, a (111) texture merely caused the magnetoresistance to progressively decay with increasing thickness of Fe_3O_4 with no sign change. This raised the question as to why the Fe_3O_4 growth orientation influenced film structural and magnetic properties and this motivated us to compare epitaxy of Fe_3O_4 (001) and (111) films grown by plasma-assisted molecular beam epitaxy.

Fe_3O_4 epitaxial growth has been reported for both (001) and (111) growth orientations by several growth techniques. Chambers[5] has given a review of epitaxial growth of iron oxides, including Fe_3O_4. For the (001) growth orientation, MgO is the most commonly used substrate because of the small lattice misfit (~ 0.4%) between the O sublattice of the two materials. However, the misfit (close to a factor of 2) between the cation sublattices tends to introduce film defects, such as antiphase boundaries [6,7]. On the other hand, there has been no report of a phase instability leading to nucleation of Fe oxide phases, other than Fe_3O_4, in

the growing film. In contrast, for the (111) growth orientation there have been several reports of formation of an interfacial iron oxide layer, of composition near FeO, in the early stages of epitaxy. For example, there is conclusive evidence[8-10] for an initial monolayer of FeO in Fe_3O_4 (111) prepared by thermal oxidation of Fe(110)/Pt(111). However, in subsequent electron microscopy analysis of films grown by this technique, Roddatis et al[11] found no trace of any phase other than Fe_3O_4. On the other hand, Gota et al [12,13] have synthesized epitaxial Fe_3O_4 using plasma-assisted MBE growth using e-beam evaporation of Fe with a coincident atomic oxygen flux. Evidence for an initial layer of FeO(111) was found using in situ reflection high energy electron diffraction which suggested that this phase persisted for several (up to 9) monolayers into the Fe_3O_4 growth. Subsequent film analysis by transmission electron diffraction[14], however, showed no evidence for any phases other than Fe_3O_4.

Measurements of the anodic oxide film grown on Fe (001) and Fe (110) show the formation of Fe_3O_4 (001)-like and Fe_3O_4 (111)-like phases, respectively. While both these films are highly defective, the defect level for Fe_3O_4(111)/Fe (110) is higher than for Fe_3O_4(001)/Fe(001), which was rationalized as due to better lattice matching in the latter case[15, 16] . In this paper we describe growth of Fe_3O_4 films, prepared under a wide range of conditions, on both MgO (001) and sapphire (0001) by oxygen plasma assisted molecular beam epitaxy. Film structural analysis confirms a phase instability in Fe_3O_4 (111) growth which leads to nanophase separation into Fe_3O_4, FeO and elemental Fe. We show that this phase separation can be entirely suppressed by selecting specific growth conditions. We also show that phase separation makes Fe_3O_4 films more difficult to magnetize than single-phase films and that film orientation strongly influences film magnetization behavior.

I. Experimental Description.

Film growth was carried out using a V80M molecular beam epitaxy system (Thermo VG Model V80M) by reactive evaporation using an e-gun (Themionics Inc) source for Fe and simultaneous impingement of O atoms from an atom source (Model HD 25, Oxford Applied Research Ltd.). Multiple substrates (including MgO(001), sapphire (0001), SiO_2/Si, a pure carbon wafer (for oxide composition and thickness determination by Rutherford back scattering) were mounted onto a single platten so that growth conditions (substrate temperature, O-atom flux etc) were identical for all substrates. Prior to sample loading, the oxide substrate wafers were immersed in a mild etchant (H_2O_2, NH_4OH, H_2O: 1:1:100), rinsed in flowing water, then introduced into the growth chamber and subjected to a flux of atomic O (240W RF power, for ~40m) during heating to 200°C. This process is known[5] to remove substrate surface impurities such as elemental carbon and CO_2. Following cleaning, samples were annealed at ~400°C and allowed to equilibrate (shuttered) at the desired growth temperature during stabilization of the O plasma prior to growth. Samples were rotated continuously, during film growth, so that all substrates were exposed uniformly to the Fe and O atom fluxes. The film growth rate was controlled by the emission current of the Fe e-gun source and measured by a calibrated quartz crystal monitor.

X-ray diffraction measurements were performed with a Rigaku 12kW rotating anode source. The CuKα X-rays were monochromatized with a bent graphite crystal and detected with 4 milliradian Söller slits. In all cases, data are plotted as a function of the scattering

vector Q, which is $(4\pi/\lambda) \sin \theta$, where λ is the X-ray wavelength (1.542 Å) and θ is half the scattering angle. The instrumental resolution is approximately $\Delta Q = 0.02$ Å^{-1}.

Films were characterized by vibrating sample magnetometry and by the magneto-optical Kerr effect (MOKE) using longitudinal geometry i.e. the magnetic field was parallel to the film plane and in the plane containing incident and reflected beams. The E vector of the polarized beam was perpendicular to the plane of incidence. A He-Ne laser was used and all measurements were made at room temperature.

Films were characterized by bright field transmission electron microscopy techniques, on cross-section foils, using a Topcon 002B microscope. Images were obtained at 100keV beam energy. Additional sample examination was made in some cases using a JEOL 2010F microscope operating at 200keV.

II. Structural analysis.

In this section we describe the results of structural analysis of films grown simultaneously on MgO(001) and sapphire(0001) substrates. Table 1 summarizes the growth parameters for a series of different growth runs covering a broad range of growth parameters. The runs are separated into different groups so that the influence of specific growth parameters can be identified. In the first group (designated GR), for example, the plasma power, background O_2 pressure and substrate temperature were held constant while the growth rate was varied. In the second group (ZP), the plasma power was zero and films were grown by reactive evaporation in molecular O_2. In the third group (VT) the substrate temperature was varied with RF power and growth rate held constant. In the remaining groups (HP, HO,) the influences of growth rate, RF power and O_2 partial pressure were

explored. Specific samples from each run are designated by the run number followed by an 'S' or an 'M' to indicate growth on a sapphire(0001) or MgO(001) substrate, respectively. All samples were examined by x-ray diffraction and some samples were also examined by transmission electron microscopy.

(a) Group 1: effect of growth rate

Considering group 1 first, the samples are listed in order of increasing growth rate. As we discuss in this section, x-ray data showed that all films grown on MgO (001) were single phase, epitaxial Fe_3O_4. On the other hand, films grown on sapphire (0001) exhibited structure and composition which depended systematically on growth rate. This is illustrated by the set of x-ray specular scans (Q normal to sample) shown in Fig 1. For the film grown at lowest rate (GR1S) the x-ray scan (Fig 1(a)) shows peaks from only α- Fe_2O_3 and the substrate. The latter peaks are labeled "s". In this case, the film has grown purely in the corundum structure α-Fe_2O_3 phase, which is trigonal, and isostructural with the substrate. The film has a single epitaxial orientation with the c-axis parallel to the film normal as expected from the moderate misfit (~6%) between in-plane lattice parameters of film and substrate.

With increasing growth rate, the film structure switched initially to single phase Fe_3O_4 and then to a phase mixture of Fe_3O_4, FeO and Fe. The specular x-ray scans for samples GR3S and GR8S, shown in Figs. 1(b) and (c), respectively, illustrate this trend. The scan shown in Fig. 1(b) for GR3S shows peaks from Fe_3O_4 (111), (222), (333) and substrate peaks only, indicating a single phase Fe_3O_4 film with Fe_3O_4 [111] oriented along the growth axis. On the

other hand, the scan (Fig. 1(c)) for sample GR8S, has peaks due to FeO(111) and metallic Fe(110) in addition to Fe_3O_4 and substrate peaks. This shows that these phases are present in the film with FeO[111] and Fe[110] directions along the growth axis. Peak fitting was used to determine the integrated intensity of Fe_3O_4 (222), FeO(111) and Fe(110) peaks. The relative integrated intensities of FeO(111) and Fe(110) peaks compared with Fe_3O_4 (222) are listed in Table 1 and are a measure of the amount of these phases in the film. It is seen that there is a general trend towards increasing amounts of these phases with increasing growth rate.

In contrast, all films in this group grown simultaneously on MgO(001) showed no evidence for phases other than Fe_3O_4. Fig. 2 illustrates this point in the case of sample GR8M. The specular scan (Fig.2 (a)) shows only a single peak at 3.0 Å^{-1} which can be assigned to an unresolved doublet of Fe_3O_4 (004) and MgO(002) . The corresponding in-plane scan (Q in the sample plane, Fig. 2(b)) shows a single peak which could be an unresolved doublet of Fe_3O_4 (400) and MgO (200). However, since this is a grazing incidence scan, most of the intensity is from Fe_3O_4. There is no evidence of any peaks, which could be assigned to FeO or Fe or γ-Fe_2O_3, and so we conclude that the film contains only epitaxial Fe_3O_4. This conclusion is supported by transmission electron microscopy studies, which will be reported elsewhere.

While the presence of additional phases is provided by x-ray diffraction, information on the location and distribution of these phases requires transmission electron microscopy. Figs. 3 and 4 show cross-section transmission electron microscopy images of samples GR3S and GR8S, respectively.

In the case of sample GR3S, the film is comprised of multiple, columnar grains. As seen in Fig. 3(a), the individual grains are distinguished by grain boundaries within the film and by the granularity in surface morphology. The grain widths for this film vary from ~100Å to ~300Å. Fig. 3(b) shows the boundary (indicated) between two grains in the Fe_3O_4 film. $(\bar{1}11)$ lattice fringes, inclined at ~70.4° to the interface, in the adjacent grains are indicated. Both grains have their [111] axis along the film normal and are related by a 180° rotation about this axis. The entire film is comprised of twinned grains of this type. The interface is flat and the higher magnification image (Fig 3 (c)) suggests a transition width of <10 Å. In agreement with the x-ray data for this film (Fig. 1(b)), no additional phases are evident.

Films grown at higher rate than 0.087Å/s on sapphire (see Table I) all showed increasing amounts of FeO and Fe. Electron microscopy images (Fig. 4) for one of these films (GR8S) reveals the distribution of these phases. Fig. 4(a) shows a dark field image of the interface region (created using sapphire (006) and Fe_3O_4 (111) diffraction spots) showing that the region (indicated by an arrow) within ~100 Å of the film-substrate interface is inhomogeneous and contains particles on the order of ~ 100 Å diameter. The selected area diffraction (SAD) pattern (Fig. 4(b)) exhibits diffraction spots, which can be assigned to epitaxial Fe_3O_4 or the sapphire substrate. The pattern confirms that the Fe_3O_4 [111] axis is along the substrate normal, sapphire [0001]. The zone axis of the SAD pattern is along sapphire [01$\bar{1}$0], which is parallel to the in-plane [112] direction of Fe_3O_4. As in sample GR3S the film is comprised of twinned grains. Diffraction spots from the additional phases are too weak to be seen in the SAD pattern, probably because of the small volume fraction of additional phases compared with the sample volume contributing to the pattern. Nevertheless, these phases can be clearly identified from the spacing of lattice fringes within particles seen in high magnification

lattice images. The ~100Å diameter particle seen in Fig. 4(c), for example, can be identified as Fe with the Fe [110] direction along the film normal. Fe and FeO particles, with Fe [110] or FeO [111] directions, respectively, along the film normal, are present mainly at the interface but in some cases within the bulk of the film. This result is entirely consistent with the x-ray data (Fig. 1(c)) for this identical sample and confirms that a nanoscale phase separation occurs primarily at the substrate–film interface but can also occur locally at regions in the bulk of the film.

(b) Group 2. Films grown by reactive evaporation of Fe in molecular O_2.

As a comparison with films grown using the plasma source a set of films was grown without the plasma source operating i.e. molecular oxygen was supplied rather than atomic oxygen. The oxygen pressure remained the same as for samples in group 1. Growth conditions and x-ray data for these films (group ZP) are listed in Table I.   Figs. 5(a) and (b), respectively, show x-ray specular scans recorded for films (ZP2S, ZP3S) grown on sapphire at identical rate (0.08Å/s) at 200 and 300 ºC. These films show peaks only from Fe_3O_4 and the substrate and are single phase. A film (ZP1S), grown at much lower rate contained a phase mixture of Fe_3O_4 and α-Fe_2O_3.

(c) Group 3: effect of substrate temperature

For the films in this group, substrate temperature had little or no systematic effect on phase purity compared with the growth rate dependence. For example sample VT1S was

grown at lower temperature (200°C) than sample GR3S (300°C) with all other growth parameters held constant. Both samples were single phase Fe_3O_4 suggesting a lowering of growth temperature had no effect on phase purity. On the other hand a comparison between sample VT6S (450°C) and samples GR6S and GR5S (300°C) of group 1 suggested that a higher growth temperature at constant rate led to single phase Fe_3O_4. This conclusion is not supported by a comparison between samples VT5S and VT3S (400°C) and sample GR3S (300°C) of group 1. In this comparison, an increased growth temperature had no effect on phase purity; all samples contained no detectable FeO and Fe. Conversely, samples VT2S (350°C) and VT4S (400°C) showed small but significant amounts of FeO and Fe, respectively, despite a growth rate less than that of sample GR3S. In general, all films in this group contained negligible or very small amounts of FeO and/or Fe.

Fig. 6 illustrates the detection by x-ray diffraction of these small amounts of additional phases. The specular scan (Fig. 6(a)) of sample VT2S shows no detectable peak from metallic Fe and no distinct peak from FeO. However, the Fe_3O_4 (111) peak shows an asymmetry with a shoulder on the low Q side indicative of a small FeO (111) component. Peak fitting confirmed the Fe_3O_4/FeO doublet with a small (0.04) integrated intensity ratio of FeO (111) to Fe_3O_4 (222). On the other hand, the specular scan (Fig.6 (b)) for sample VT4S showed no asymmetry of the Fe_3O_4 (111) peak but a weak Fe (110) peak (indicated). Cross-section transmission electron microscopy images of this sample (Fig. 7(a) and (b)) confirmed the presence of nanoparticles at the sapphire/film interface with a separation of ~1000Å. The spacing of lattice fringes (seen in Fig. 7(b)) within the particles, measured using an optical diffractogram of the image, was ~2 Å consistent with the Fe (110) fringe spacing in bcc Fe.

One sample of this group, (VT7S) was prepared under conditions of a higher temperature (450ºC) and much lower growth rate than the other samples of this group in an attempt to replicate the growth conditions, for Fe_3O_4 / sapphire (0001), stated by Gota et al.[12,13]. The Gota et al conditions were a substrate temperature of 450ºC, rate of ~0.035Å/s and an *electron cyclotron resonance* plasma source operating at 350W. The specular scan for this sample (Fig. 6(c)) shows that the film is comprised predominantly of epitaxial α-Fe_2O_3 with its hexagonal c-axis parallel to the substrate c-axis. The remainder of the film is comprised of Fe_3O_4 as shown by weak but significant peaks corresponding to Fe_3O_4(111), (222) and (333). No peaks from FeO or metallic Fe were present for this sample. Fig. 8(a) shows a lattice image of the cross-section of this sample. In this image, parallel sets of (01$\bar{1}$2) lattice fringes (indicated) run from the sapphire substrate across the interface into the film. This confirms that the film structure, in this region of the interface, is α-Fe_2O_3 and there is local in-plane registry between the film and substrate. Careful inspection reveals the interface is in fact semi-coherent and contains edge dislocations to accommodate the in-plane misfit between the film (in-plane O-O spacing 2.92Å) and substrate (O-O in-plane spacing 2.75Å). The Fe_3O_4 minority phase in this sample is distributed in localized regions along the interface. Fig. 8(b) shows a lattice image of a region where a region of Fe_3O_4 about 250Å across is nucleated at the interface. The nucleation of the Fe_3O_4 does not appear to induce twinning or other defects into the α-Fe_2O_3 majority phase. We note that the growth conditions for this film are at or close to the Fe_3O_4 - Fe_2O_3 phase boundary.

(d) Group 4: effect of increased RF power and O_2 pressure.

The final group of samples (HP) was prepared with an increased RF power (260W) at temperatures from 250 to 400°C and at higher O_2 pressure. For this group, as for group 1, the growth rate played a controlling influence on the film phase. The first run (HP1) of this group had a similar growth rate to runs GR3 and GR4 of group 1 but the more strongly oxidizing growth conditions led to growth of a single phase α-Fe_2O_3 film (HP1S) on sapphire and to a γ- Fe_2O_3 film (HP1M) on MgO (001). Figs. 9(a)-(c) show x-ray scans for these samples. The specular scan (Fig. 9(a)) of the film on sapphire shows only α-Fe_2O_3 and substrate peaks while the specular scan (Fig. 9(b)) of the film on MgO(001) shows a dominant peak which is a superposition of MgO(002) and a peak which could be assigned to either Fe_3O_4 or γ-Fe_2O_3(004) peaks. However, the in-plane scan (Fig. 9(c)) of this film shows the characteristic (110)-superstructure peak of γ-Fe_2O_3 with intensity consistent with a single phase. It is interesting that this is the only sample in which the structure of the film on MgO(001) assumed a different structure than Fe_3O_4. This suggests that, under sufficiently strongly oxidizing growth conditions, films of the highest oxidation state (i.e. Fe_2O_3) are formed, irrespective of substrate and lattice-matching conditions.

A comparison of the data (Table I) for samples HP2S vs GR8S vs HP3S illustrate the controlling influence of growth rate. Films HP2S and GR8S were grown at similar and high rates (at 300°C) and both films contain a large fraction of FeO. The more strongly oxidizing growth conditions for sample HP2S appears to eliminate the Fe content of the film. Fig. 10(a) shows a specular x-ray scan for this sample, illustrating this point. Film HP3S, grown at a higher temperature (400°C), contains both FeO and Fe (see Fig 10(b)) showing that growth at a higher temperature does not result in a single-phase film at this high growth rate. Single-phase growth requires a relatively low growth rate at 400°C as is the case at 300°C.

III Magnetic Properties

MOKE loops were recorded for single-phase Fe_3O_4 films and mixed phase films containing Fe_3O_4 with FeO and Fe. Fig. 11(a) compares MOKE loops for single phase films grown on both MgO (001) and sapphire (0001) substrates at a substrate temperature of 300°C. The Fe_3O_4 (111) film showed no angular dependence of loop shape or coercivity as the field was applied along different in-plane directions. This is seen from the near-identical loops for in-plane azimuths ([110], [211]) differing by 30°. This characteristic was common for all (111) films. On the other hand, Fe_3O_4(001) films exhibited 4-fold magnetic anisotropy with easy directions along Fe_3O_4 [110] and [$\bar{1}$10] and hard directions along Fe_3O_4 [100] and [010] directions. All Fe_3O_4 (111) films were more difficult to magnetize compared with Fe_3O_4 (001) films formed under identical growth conditions. This is illustrated by the smaller remanence, larger coercivity and higher saturation field for the (111) film compared with the (001) film in Figs. 11(a)-(d). This large coercivity difference is present for all growth temperatures as shown by the data of Fig. 12. The significant increase in coercivity for (001) films grown at 400 and 450°C is probably related to interdiffusion between film and substrate as reported by Lind et al[17].

The effect of phase separation on magnetic properties of (111) films was evident from a comparison of MOKE loops for pure and mixed phase films. For example, mixed phase films (GR4S, GR5S, GR6S), grown at a substrate temperature of 300°C, all showed significantly higher coercivity compared with a single-phase film (GR2S) grown at the same temperature. The data points for these films, summarized in the coercivity vs growth temperature plot in Fig. 12, illustrate this. In the case of sample GR7S, which was largely FeO, the MOKE response was very weak and anomalous indicating a much-reduced magnetization. M-H

loops for this sample, recorded using vibrating sample magnetometry in an applied field up to 15kOe, confirmed a reduced magnetization and lower remanence compared with sample GR2S. These data are shown in Fig. 13 (a). M-H loops for samples GR2S, GR2M (easy axis) and GR7S are compared in Figs. 13(b and c). In these figures, the moment values are normalized to the high field (15kOe) values for each sample. The data confirm the much lower coercivity, higher remanence and faster approach to magnetization for the film grown on MgO. The slower approach to saturation for the mixed phase film (sample GR7S) is also evident. Here we note that for sample GR2M the absolute value of the moment is 331 ± 30 emu/cc at 100 Oe , increasing to 390 ± 30 emu/cc at 15 kOe. These values correspond to 71% and 83% of the magnetization (471 emu/cc) of bulk magnetite. A more complete study of high-field magnetization behavior of epitaxial (001) films will be presented elsewhere.

Discussion.

The present study of Fe_3O_4 (111) film growth appears to be the first in which FeO and Fe precipitates have been identified by *post-growth* analysis in films prepared under specific growth conditions. In prior studies by Gota et al [12,13], using plasma-assisted molecular beam epitaxial growth, a layer of FeO was detected in the growth of the first few monolayers using in situ RHEED. However, post-growth film analysis by transmission electron microscopy[14] of a ~100Å-thick film revealed no evidence for FeO in the first few monolayers. Similarly, the growth of Fe_3O_4 (111) on Pt(111), by high temperature oxidation of Fe in molecular O_2, is known[8-10] to begin with an initial wetting layer, structurally similar to FeO. On the other hand, no evidence for this layer was found in post-growth analysis[11], by transmission

electron microscopy, of films prepared by this technique; the interface appeared chemically abrupt with no evidence for any phase other than Fe_3O_4

A major difference between these earlier studies and the present work is that the growth rate dependence of film structure, in Fe_3O_4 (111) growth, was not previously studied. For example, in the work of Gota et al[12,13], the growth rate was fixed at 0.035 Å/s and the substrate temperature was used as the growth variable which controlled the film phase to be either α-Fe_2O_3 (250°C) or Fe_3O_4 (450°C). Gota et al used a different type of oxygen plasma source from ours, operating at a different power, and so growth conditions are not identical to the present conditions. Nevertheless, at a growth rate of 0.035 Å/s Gota et al found no evidence for FeO or Fe precipitates in the Fe_3O_4 film. At a similar growth rate, we also found no FeO or Fe precipitates in our samples; films grown at 300°C (GR1S) or 450°C (VT7S)) were pure α-Fe_2O_3 or predominantly α-Fe_2O_3, respectively. Chambers et al [18], on the other hand, have found a clear signature of metallic Fe in XPS studies of Fe_3O_4 (111) films grown by molecular beam epitaxy on MgO(111) from an electron cyclotron resonance source (for O and an e-gun evaporation source for Fe) operating under conditions which produced single phase epitaxial Fe_3O_4 (001)/MgO(001). Again, this result is consistent with our data in that the growth rate (1.3 Å /s) used by Chambers was higher than used by Gota et al and in our work. Thus it is clear that growth rate is a controlling factor in the formation of Fe and FeO precipitates.

Fig. 14 shows a growth phase diagram summarizing the dependence of film phase on growth temperature and growth rate from our data (Table I). The transitions of film structure from α-Fe_2O_3 to single phase Fe_3O_4 to mixed phase films is clear from the data at a growth temperature of 300°C. We note that since the film growth rate is controlled by the Fe

evaporation rate, the flux ratio of Fe to molecular O_2 and O atoms increases with growth rate. (We have confirmed that film growth rate varies linearly with the Fe evaporation rate over the entire range of growth rates in our data set). Thus there is a trend towards more strongly oxidizing conditions with decreasing growth rate that is consistent with the observed structure transitions. The approximate phase boundary between α-Fe_2O_3 and Fe_3O_4 is indicated by the dashed line which passes through the data point for the mixed phase α-Fe_2O_3 + Fe_3O_4 film (VT7S). In this diagram we have included a data point from the pure phase α-Fe_2O_3 film (HP1S) grown at a higher O_2 pressure (and consequently lower growth rate/ O_2 pressure ratio) than for all the other samples in the plot. The point is plotted at a growth rate scaled by the ratio in O_2 growth pressures so that it can be compared with the other data points to help define the phase boundary. We also show an approximate phase boundary between pure phase Fe_3O_4 and the mixed phase regime in which FeO and/or Fe is present.

One possible mechanism for incorporation of FeO and Fe into the films, grown at higher rates, is that FeO nucleates initially in the first few monolayers as established by Gota et al. FeO, however, is thermodynamically unstable at temperatures *below* 580°C and is known[19] to dissociate into Fe_3O_4 and Fe products. At our growth temperatures (<450°C), It will then tend to dissociate. However, dissociation may be incomplete at high enough growth rates because subsequent overlayers will tend to trap the products. In contrast, at sufficiently low growth rates, dissociation may be complete and the products incorporated into the Fe_3O_4 film. For example, Fe_3O_4 could be incorporated directly while the Fe product could be oxidized (to Fe_3O_4) and then incorporated. Under the lowest growth rate conditions, at which single phase α-Fe_2O_3 forms, the dissociation products could both become oxidized to α-Fe_2O_3 and incorporated. On the other hand, at high growth rates, there may be insufficient

time for complete dissociation of FeO, or for oxidation of the products, before further overlayers are deposited. We also note (from a comparison between data from samples HO1S and GR5S) that the use of higher O_2 pressure (all other growth parameters remaining identical) can inhibit FeO formation in the film. This may be due to oxidation of FeO and Fe products.

A comparison between the data of groups 1 and 2 show that it is possible to prepare single phase Fe_3O_4 without the need for a plasma source of atomic oxygen. However, the comparison also shows that single phase $\alpha\text{-}Fe_2O_3$ is not formed in molecular O_2 even at the lowest (0.037Å/s) growth rate. Growth of single-phase $\alpha\text{-}Fe_2O_3$ requires impingement of atomic O.

The dominant influence of the substrate on the phase diagram is evident from the fact that up to the highest growth rate (0.136Å/s) of the present experiments, single phase epitaxial Fe_3O_4 (001) formed on MgO (001) but mixed phase films formed on sapphire (0001) under identical growth conditions. The phase diagram for growth on MgO is thus very different from growth on sapphire (0001). For example, along the 300°C line, from 0.037Å/s to 0.136Å/s, Fe_3O_4 was the only phase found on MgO (001). The transition from Fe_3O_4 to $\gamma\text{-}Fe_2O_3$ on MgO(001) required more strongly oxidizing conditions such as those for sample HP1M (plasma power 260W/P(O_2)=6.6mb and a substrate temperature of 250°C. This strong influence of substrate on film composition is analogous to a similar effect found[20] in growth of epitaxial III-V compound alloy films and for the anodic oxidation of Fe mentioned earlier. Lattice matching between the substrate and a film of a specific composition tends to stabilize the lattice-matched composition despite variations in incident flux composition. The driving force for this so called "composition pulling" effect is a lowering of interfacial energy.

The phase instability in Fe_3O_4 (111) film growth may have significant implications for very thin (<100Å-thick) films in magnetic tunnel junctions. For a nanoscale, phase-separated Fe_3O_4 film, intended as a spin-polarizing electrode in an MTJ application, current may tend to flow from the metallic Fe precipitates into the barrier. This inhomogeneity could defeat the spin-polarizing properties of the electrode. We find that in-plane resistivity data for Fe_3O_4 films, exhibiting phase separation, often reveals lateral percolation of current through the Fe precipitates.

Magnetic data, shown in Figs. 11-13, show that single-phase Fe_3O_4 (111) films are more difficult to magnetize compared with Fe_3O_4(001) films formed under identical growth conditions. This probably reflects the higher density of film defects in Fe_3O_4 (111) films due to the absence of in-plane lattice matching as well as the presence of twin boundaries. In addition, phase separation introduces significant changes in magnetic properties e.g. increases in coercivity or reduced moment as shown by the data of Figs. 12-13. The origin of these changes is complex since phase separation introduces a distribution of nanoscale metallic Fe and/or FeO into the films. FeO in bulk, is known[19] to be a low temperature antiferromagnet (T_N = ~198K) and probably a spin glass at room temperature. This may explain the reduced moment of sample GR7S, which is predominantly FeO. On the other hand, the increased coercivity seen in other mixed-phase films may be due to structural defects in the majority Fe_3O_4 phase introduced at interphase boundaries. Thus both the orientation and phase separation effects contribute to difficulty in saturation of magnetization, which in turn may contribute to the attenuation of magnetoresistance in magnetic tunnel junctions incorporating (111) textured Fe_3O_4 films.

Finally, we note that the results of this paper are consistent with a very recent report by Hu et al [21] of negative spin polarization of epitaxial Fe_3O_4 (110) films in magnetic tunnel junctions. The Fe_3O_4 films were lattice-matched to a spinel-structure $CoCr_2O_4$ layer/$SrTiO_3$ (110) and so phase separation is not expected in this case.

Summary

We report a phase instability in growth of Fe_3O_4 (111) films in which nanoscale phase separation into a mixture of Fe_3O_4, FeO and Fe occurs under a wide range of growth conditions. We suggest that the instability is due to formation of FeO in the early stages of growth. The phase separation can be completely suppressed by selecting appropriate growth conditions. The magnetic properties of Fe_3O_4 films depend strongly on growth orientation and on the phase separation. Fe_3O_4 (111) films, whether single or mixed phase, are much more difficult to magnetize compared with Fe_3O_4 (001) films grown under identical conditions.

References

1. Z. Zhang, S. Satpathy, Phys. Rev. B **44**, 13319 (1991).

2. A. Freeman, personal communication. Unpublished.

3. A. F. Panchula, S.S.P. Parkin, Paper presented at the March Meeting of American Physical society, Seattle, Washington (2001).

4. S.S.P. Parkin, C. Kaiser, A. F. Panchula, unpublished.

5. S.A. Chambers Surface Science Reports, **39**, 105 (2000).

6. D. T. Margulies, F.T. Parker, M.L. Rudee, F.E. Spada, J.N. Chapman, P.R. Aichison, A.E. Berkowitz, Phys. Rev. Lett. **79**, 5162 (1997).

7. J.M. Gaines, P.J.H. Bloemen, J.T. Kohlhepp, C.W.T. Bulle-Lieuwma, R.M. Wolf, A. Reinders, R.M. Jungblut, P.A.A. van der Heijden, J. T.W.M. aan de Stegge, W.J.M. de Jonge Surf. Sci. **373**, 85 (1997).

8. J. Kim, C. Westphal, R.X. Ynzunza, Z. Wang, H.C. Galloway, M. Salmeron, M.A. Van Hove, C.S. Fadley, Surf. Sci. **416**, 68 (1998).

9. M. Ritter, W. Weiss, Surf. Sci. **432**, 81 (1999).

10. Sh. K. Shaikhutinov, Y. Joseph, C. Kuhrs, W. Ranke, W. Weiss, Faraday. Discuss. **114**, 439(1999).

11. V.V. Roddatis, D.S. Su, C. Kuhrs, W. Ranke, R. Schlögl, Thin Solid Films **396**, 78 (2001).

12. S. Gota, E. Guiot, M. Henriot, M. Gauthier-Soyer, Physical Review B **60**, 14387 (1999).

13. S. Gota, Surface Science **454-456**, 796 (2000).

14. S. Gota, personal communication. Unpublished.

15. M.F. Toney, A.J. Davenport, L.J. Oblonsky, M.P. Ryan, C.M. Vitus, Physical Review Letters **79**, 4282 (1997)

16. A.J. Davenport, L.J. Oblonsky, M.P. Ryan, M.F. Toney, J. Electrochem. Soc. **147**, 2162 (2000).

17. D. Lind, K.A. Shaw, E. Lochner, D.M. Lind, J. Appl. Phys. **87**, 1727 (2000).

18. S.A. Chambers, personal communication. Unpublished.

19. Landolt-Börnstein, New Series, Group III, Volume 4, Part a, pp3-7. Published by Springer- Verlag, Berlin (1970)

20. K. Hiramatsu, Y. Kawaguchi, M. Shimizu, N. Sawaki, W. Taki, N. Kuwano, K. Oki, MRS Internet Journal of Nitride Research, **2**, article 6 (1997)

21. G. Hu, Y. Suzuki, in press, Physical Review Letters

Figure captions

1. Specular x-ray scans of films grown on sapphire (0001) substrates. The films have identical growth parameters (RF power 220W, O_2 pressure 4 mb, substrate temperature 300°C) but different growth rate. CuKα radiation.

   (a) Sample GR1S: growth rate 0.037Å/s

   (b) Sample GR3S: growth rate 0.087 Å /s

   (c) Sample GR8S: growth rate 0.136 Å /s

2. x-ray scans for Fe_3O_4 film grown on MgO(001) substrate (sample GR8M). Film grown simultaneously with sample GR8S. Only peaks from Fe_3O_4 and the substrate are present.

   (a) specular scan

   (b) in-plane scan

3. (a) – (c) Cross-section transmission electron micrographs of sample GR3S at increasing magnification. The cross-section images are viewed along the [10 $\bar{1}$ 0] zone axis of sapphire.

4. Cross-section transmission electron micrographs and selected area diffraction pattern for sample GR8S

   (a) dark field image

(b) SAD pattern

(c) High magnification image of film/substrate interface

5. Specular x-ray scans of Fe_3O_4 films grown on sapphire (0001) substrates by reactive evaporation in molecular O_2 (RF power=0).

   (b) sample ZP2S: substrate temperature 200°C, rate 0.084 Å /s

   (c) sample ZP3S : substrate temperature 300°C , rate 0.083 Å /s

6. Specular x-ray scans of Fe_3O_4 films grown on sapphire (0001) substrates.   The films were grown with identical RF power (220W) but at different substrate temperatures. CuKα radiation.

   (a) sample VT2S: Ts=350°C, rate 0.083 Å /s

   (b) sample VT4S: Ts=400°C, rate 0.082 Å /s

   (c) sample VT7S: Ts=450°C, rate 0.024 Å /s

7. Cross-section transmission electron micrographs of Fe_3O_4 films grown on sapphire (0001) substrates. Growth conditions specified in Fig. 6 captions.

   (a) sample VT4S, low magnification image

   (b) sample VT4S, high magnification image showing Fe (220) lattice fringes within interfacial bcc Fe nanoparticle

8.   (a) sample VT7S: high magnification image showing semi-coherent interface between substrate and α-Fe_2O_3 majority phase

(b) sample VT7S, high magnification image of interface region showing a region of Fe_3O_4 between substrate and α-Fe_2O_3 majority phase.

9. X-ray scans of films (HP1S and HP1M, respectively) grown simultaneously on (a) sapphire (0001) and (b), (c) MgO (001) substrates under conditions of Fe_2O_3 phase stability (RF power 260W, Ts=250°C, growth rate 0.090 Å /s). Scans in (a) and (b) are specular scans. The scan in (c) is an in-plane scan showing the (110) superstructure peak from γ-Fe_2O_3.

10. Specular x-ray scans of films grown on sapphire (0001) substrates at 260W RF power.

    a. HP2S: Ts=300°C, rate 0.139 Å /s

    b. HP3S: Ts=400°C, rate 0.134 Å /s)

11. (a)-(d) Longitudinal MOKE loops for films of single-phase Fe_3O_4 grown simultaneously on sapphire(0001) and MgO(001) substrates. The in-plane directions of the applied field are indicated. (a) and (b) sample GR2S ; (c) and (d) sample GR2M.

12. Coercivity vs growth temperature for single-phase films ($\circ$-(111); $\square$- (001)) grown simultaneously on sapphire(0001) and MgO(001) substrates. Sample numbers indicated. Coercivity values for mixed phase films are indicated by the data points: Δ (sample GR4S); $\Diamond$ (sample GR5S); ∇ (sample GR6S).

13. (a) M-H loops for samples GR7S (predominantly FeO(111))-dotted line and GR2S (single-phase Fe_3O_4 (111))-solid line. The moment comparison takes into account differences in film thickness and area for the two samples.

(b) M-H loops for samples GR7S -dotted line; GR2S-solid line; GR2M-dashed line. The moments are normalized to the values at 15 kOe for each sample.

(c) M-H loops for samples in (b) over the field range -1kOe to 1 kOe.

14. Phase diagram, showing dependence of film phase on growth temperature and growth rate for growth of iron oxide on sapphire (0001). ∇- pure phase α-Fe_2O_3 (0001) ; $\blacktriangledown$ - mixed phase α-Fe_2O_3 (0001) and Fe_3O_4 (111) ; $\triangle$ - pure phase α-Fe_2O_3 (0001) but data point scaled for different ratio of growth rate / O_2 growth pressure for this point. $\square$-pure phase Fe_3O_4 (111); $\circ$-mixed phase films containing Fe_3O_4 with FeO and/or metallic Fe.

TABLE I. Summary of film growth conditions and normalized integrated x-ray diffraction intensities for Fe-oxide films on sapphire (0001)

	Growth conditions					Normalized integrated intensities[†]			
Sample #	RF power W	$P(O_2)$ 10^{-6} mb	T_G °C	Growth rate Å / s	Thickness Å	FeO (111)	Fe_3O_4 (222)	Fe (110)	$\alpha\text{-}Fe_2O_3$ (00.6)
GR1	220	4.1	300	0.037	259±20				1
GR2	220	4.2	300	0.065	365±30		1		
GR3	220	4.2	300	0.087	448±30		1		
GR4	220	4.1	300	0.090	338±30	0.06	0.93	0.01	
GR5	220	4.2	300	0.103	350±30	0.38	0.61	0.01	
GR6	220	4.1	300	0.101	436±30	0.68	0.31	0.01	
GR7	220	4.1	300	0.121	343±30	0.93	0.06	0.01	
GR8	220	4.0	300	0.136	797±30	0.39	0.57	0.04	
ZP1	0	4.2	300	0.037	267±20		0.03		0.97
ZP2	0	4.1	200	0.084	323±30		1		
ZP3	0	4.2	300	0.083	345±20		1		
ZP4	0	4.2	300	0.081	346±20		1		
VT1	220	4.1	200	0.082	370±30		1		
VT2	220	4.1	350	0.083	294±30	0.04	0.96		
VT3	220	4.2	400	0.072	397±30		1		
VT4	220	4.1	400	0.082	416±30		0.99	0.01	
VT5	220	4.1	400	0.088	407±30		1		
VT6	220	4.1	450	0.104	347±30		1		
VT7	220	4.1	450	0.024	233±20		0.02		0.98
HP1	260	6.6	250	0.090	284±10		0		1
HP2	260	5.0	300	0.139	347±30	0.53	0.47		
HP3	260	5.0	400	0.134	343±30	0.06	0.87	0.07	
HO1	220	7.0	300	0.102	365±30		1		

† a null entry denotes no detectable peak i.e. below 1% of dominant peak
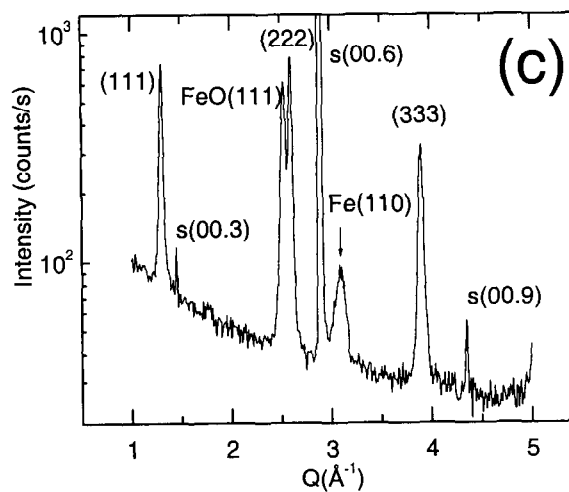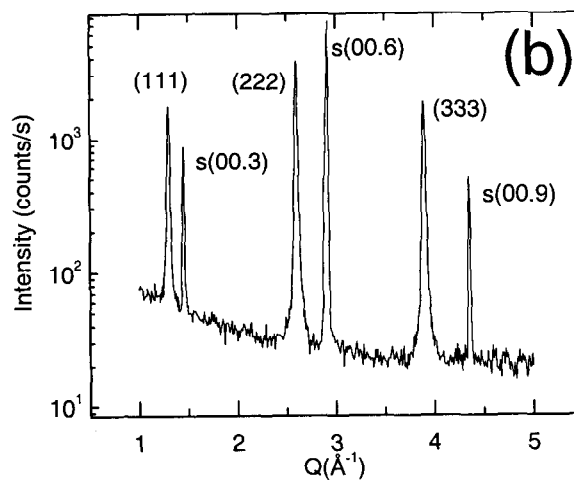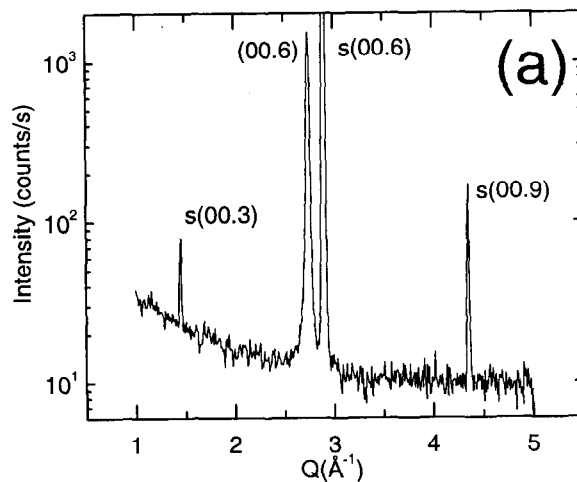
Figure (a), (b), (c) — X-ray diffraction spectra of Intensity (counts/s) versus $Q(Å^{-1})$.

(a): s(00.3), (00.6), s(00.6), s(00.9)

(b): (111), s(00.3), (222), s(00.6), (333), s(00.9)

(c): (111), s(00.3), FeO(111), (222), s(00.6), Fe(110), (333), s(00.9)

Farrow
Fig 1

(a) Fe₃O₄ / α-Al₂O₃ — 250 Å

(b) — 50 Å

(c) — 25 Å

Farrow
Fig 3

(a) Fe₃O₄

α–Al₂O₃

100Å

(b)

333f
006s
104s
111f
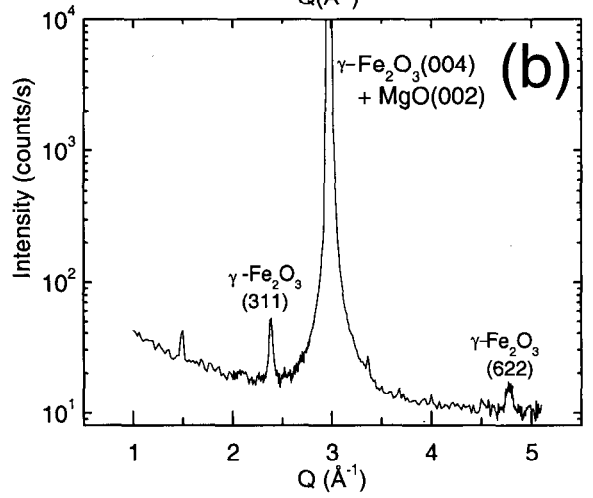311f
202s
220f 440f 300s
102s
311f
204s

(c)

Fe

50 Å
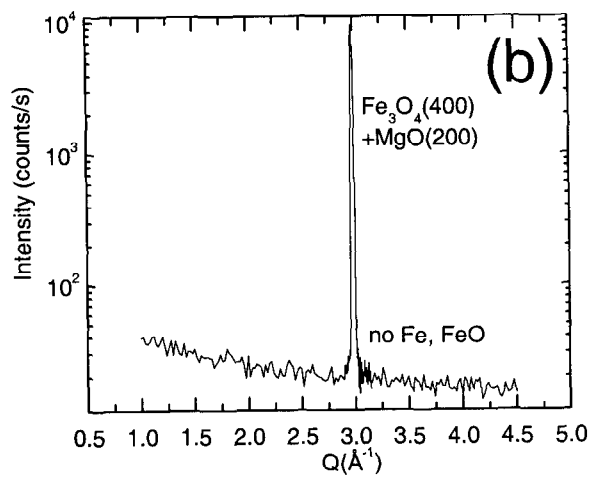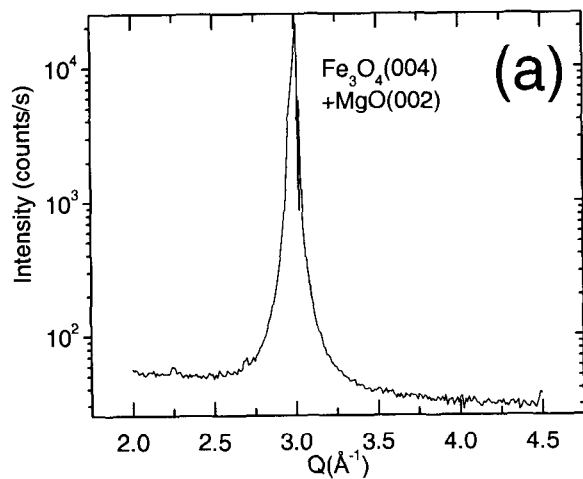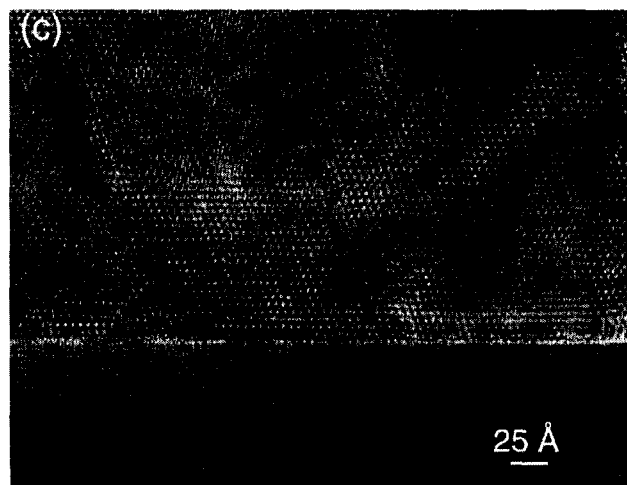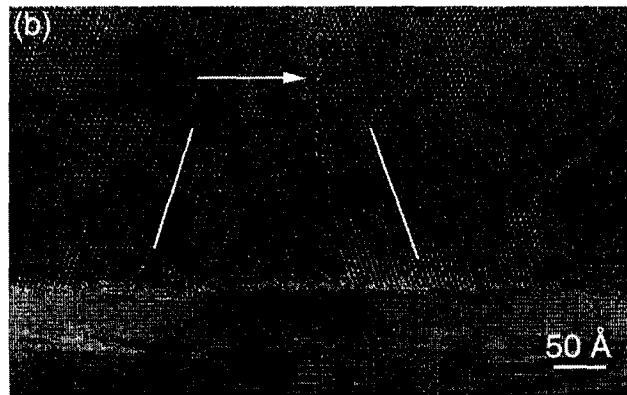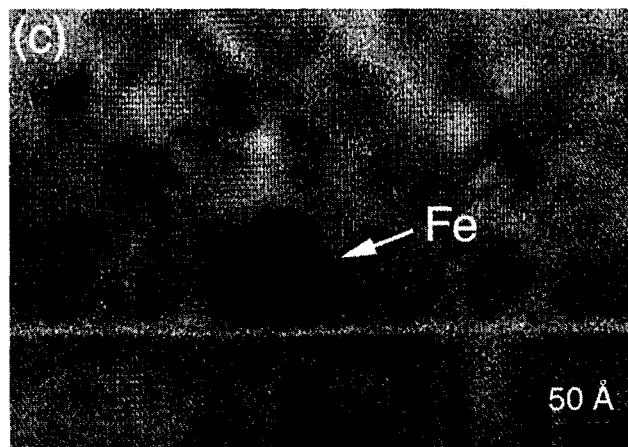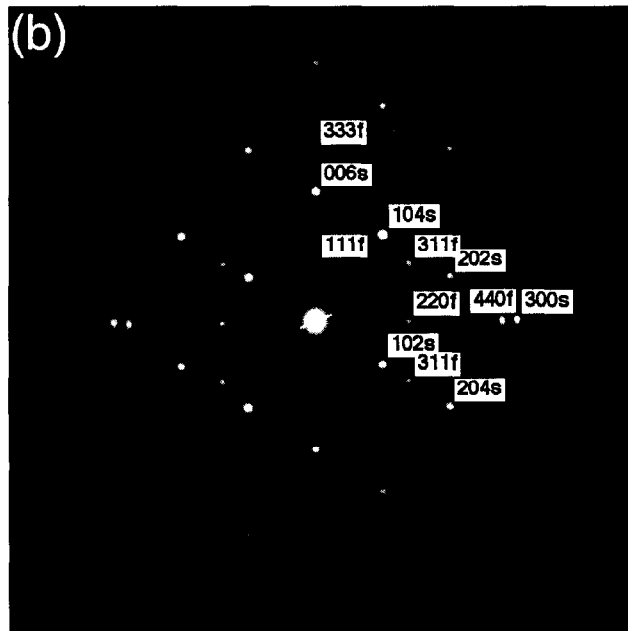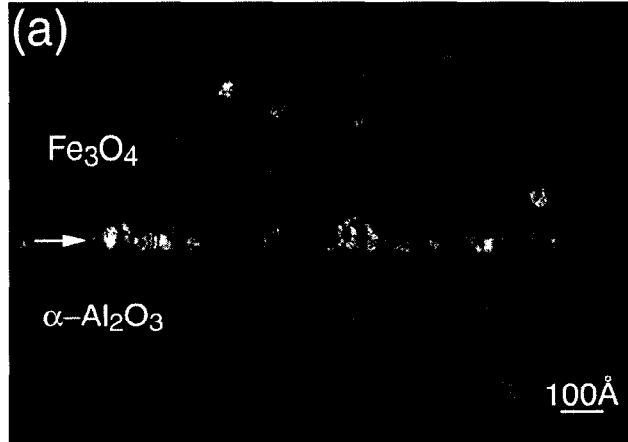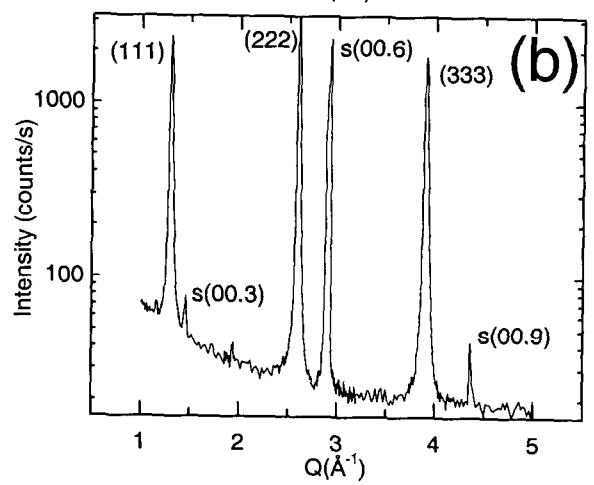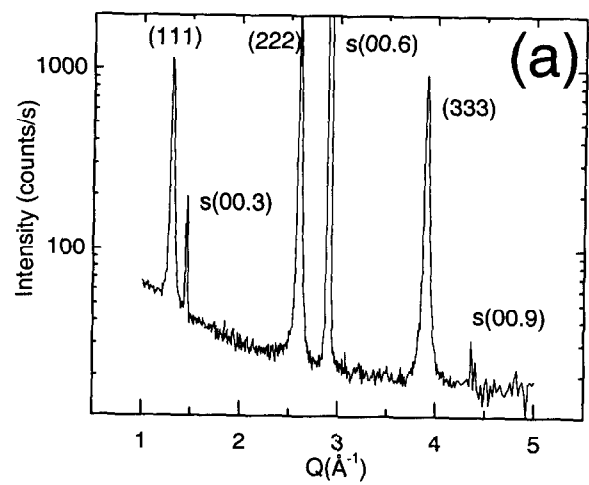
Farrow
Fig 4

Farrow
Fig 5

Farrow
Fig 6

(a)

Fe₃O₄

Fe

α–Al₂O₃

100 Å

(b)

Fe(220)

25 Å

Farrow
Fig 7

(a)

α–Fe$_2$O$_3$

α–Al$_2$O$_3$

25 Å

(b)

α–Fe$_2$O$_3$

Fe$_3$O$_4$

α–Al$_2$O$_3$

50 Å
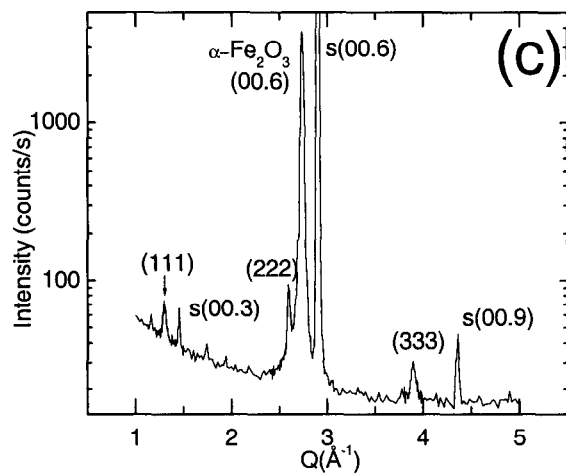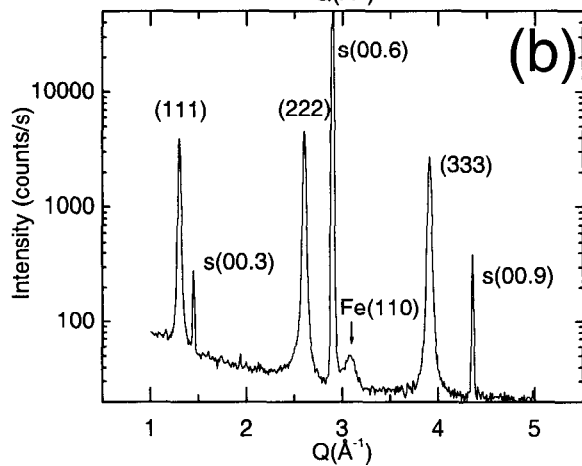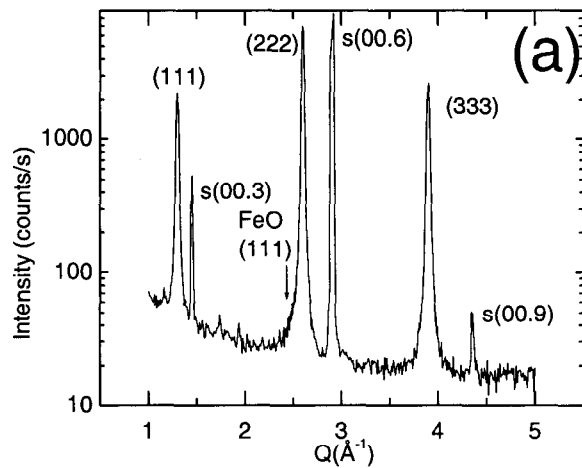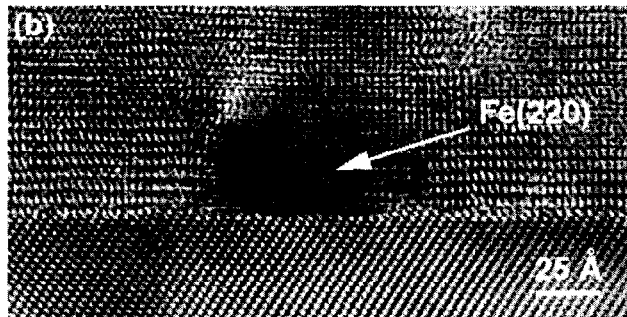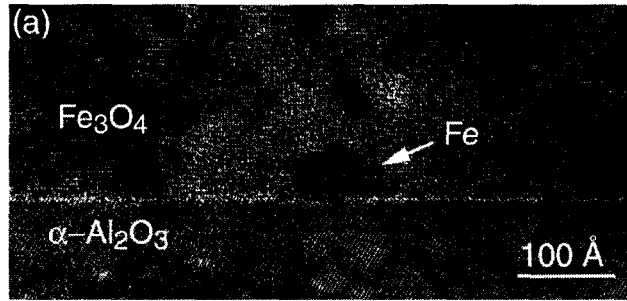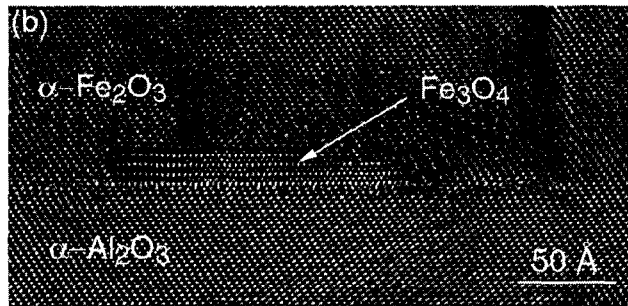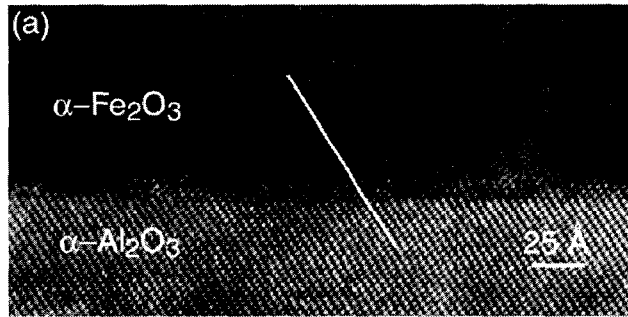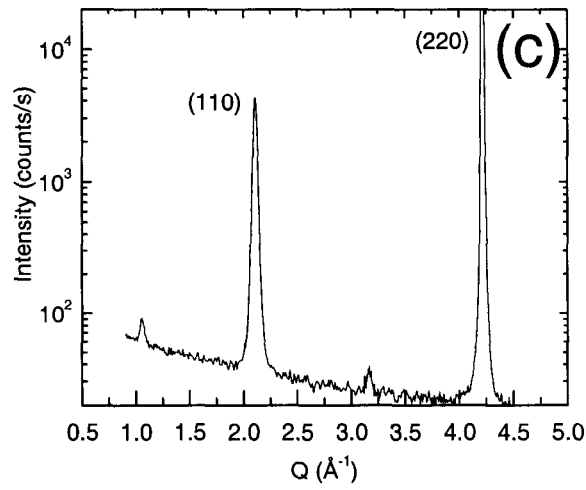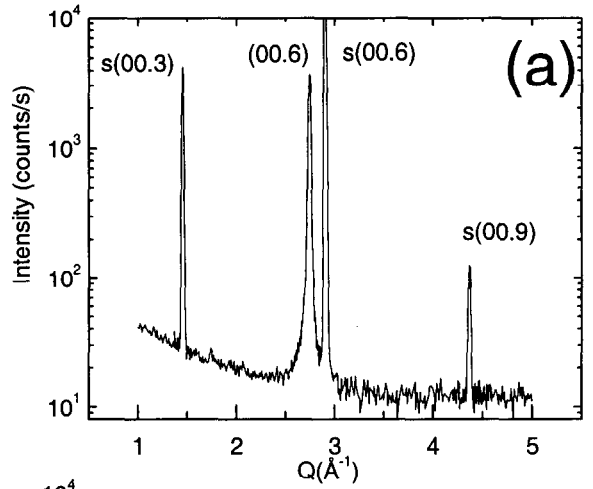
Farrow
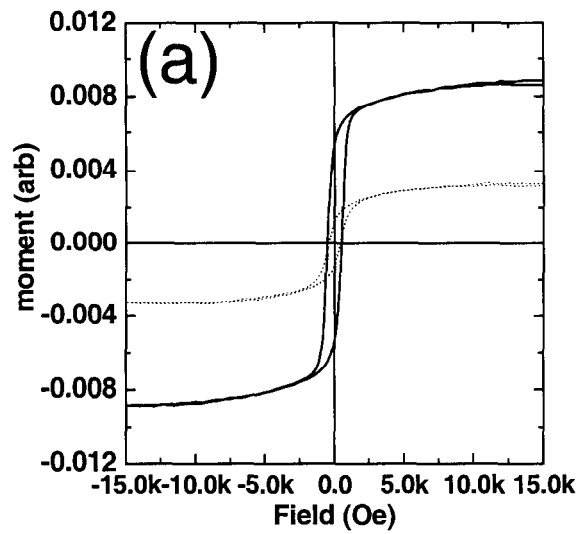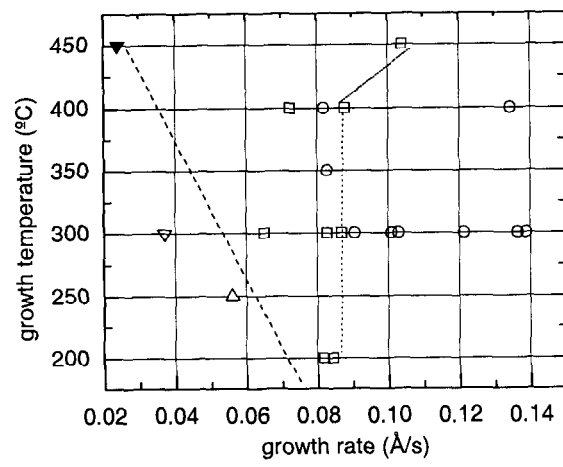Fig 8
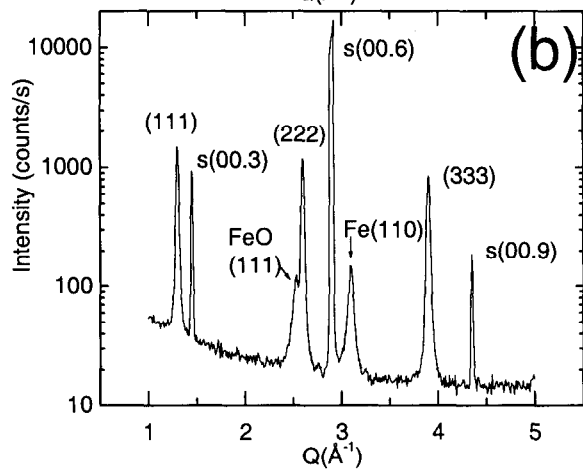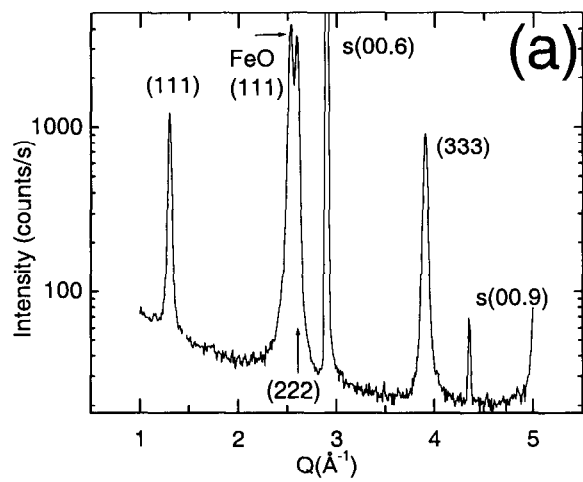
Farrow
Fig 9

Farrow
Fig10
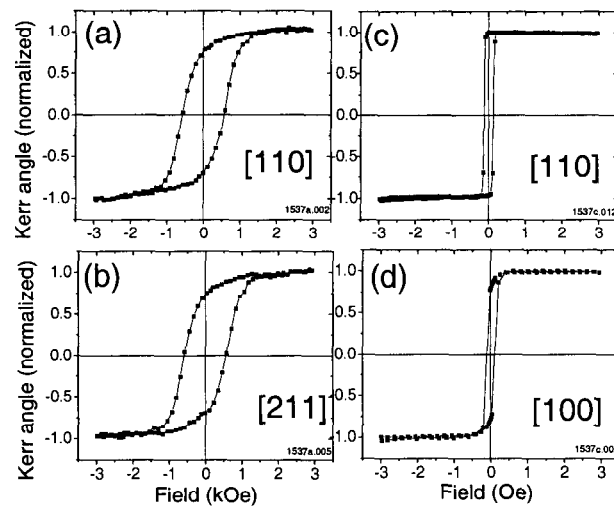
Farrow
Fig 11
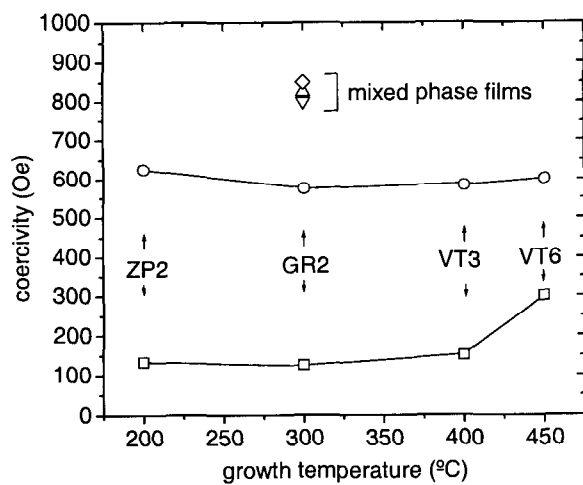
Farrow
Fig 12

Fig 13

Fig 14